This is a repository copy of *Individual effect of recrystallisation nucleation sites on texture weakening in a magnesium alloy: Part 2- shear bands*.

White Rose Research Online URL for this paper:
https://eprints.whiterose.ac.uk/125478/

Version: Published Version
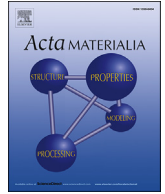
Full length article

Individual effect of recrystallisation nucleation sites on texture weakening in a magnesium alloy: Part 2- shear bands

Dikai Guan[*], W. Mark Rainforth[**], Junheng Gao, Le Ma, Brad Wynne

Department of Materials Science and Engineering, University of Sheffield, Sheffield S1 3JD, UK

A B S T R A C T

The entire recrystallisation process of a cold-rolled WE43 Mg alloy containing a high density of shear bands was tracked using a *quasi-in-situ* electron backscatter diffraction method. The results showed the resultant recrystallised texture arose principally from recrystallisation within shear bands rather than from deformation twins, which made a negligible contribution to the final texture. Only a weakened basal texture with scattered weak texture components was observed after annealing at 450 °C and 490 °C. This is in contrast to the widely reported "Rare Earth" textures, believed to come from shear band recrystallisation. The texture appeared during the nucleation of recrystallised grains and was preserved during subsequent grain growth. Simultaneous occurrence of precipitation on grain and twin boundaries during recrystallisation suppressed any potential preferential grain growth. When annealed at 545 °C, at which temperature both solute drag and Zener pinning were eliminated, a non-basal texture was produced after annealing due to orientated grain growth governed by different grain boundary mobility between basal and off-basal grains.

1. Introduction

A strong basal crystallographic texture is usually produced after cold rolling or thermomechanical processing in Mg and Mg alloys [1—5]. Subsequent annealing is not effective in modifying this texture in conventional rare earth free Mg alloys [6,7]. However, Mg alloys containing rare earth additions (Mg-RE alloys) commonly exhibit only a weak basal texture due to the introduction of the "Rare Earth texture" (RE texture) [8], which forms either during thermomechanical processing or subsequent annealing [1,8—13]. Frequently reported RE textures are the $<11\bar{2}1>$//ED(extrusion direction) produced after extrusion [8], and peak texture intensity reduced and tilted towards the transverse direction (TD) after rolling and/or subsequent annealing [2,14—16].

Although RE textures have been widely reported over the past two decades, the mechanism of RE texture formation remains a matter of much debate. Numerous mechanisms have been proposed, with the proposed key factors including the choice of preferential nucleation sites [2,4,8,9,11,17—20], increased activity of

pyramidal <c+a> slip [5], oriented grain growth and solute drag or particle pinning along some specific grain boundaries (GBs) [21—25]. It is challenging to validate all the aforementioned proposed mechanisms. Nevertheless, a key issue to understanding the RE texture is to understand the location of the nucleation site(s) and/or subsequent growth of corresponding recrystallised grains that lead to the formation of a RE texture. In an accompanying paper [20] the individual effect of recrystallisation sites, in particular double twins, on the weakening of the texture in WE43 alloy were systematically investigated. The results unequivocally demonstrated that recrystallisation within double twins was the main contribution to the final RE texture. The RE texture appeared at the nucleation stage and was retained during the subsequent uniform grain growth. However, the material had been processed to specifically exclude shear banding from the structure and to promote twinning as the main deformation mechanism. Therefore, the study did not answer the question as to whether shear bands can also form the RE texture in WE43 alloy when other nucleation sites, including second phase particles and deformation twins, are excluded?

Shear bands are narrow zones of intensive shear strain providing a wide range of internal misorientations. A wide spectrum of orientations can be generated during dynamic and static recrystallisation [1,4,8,10,15,21]. It is widely accepted that RE

* Corresponding author.
** Corresponding author.
E-mail addresses: dikai.guan@sheffield.ac.uk (D. Guan), m.rainforth@sheffield. ac.uk (W.M. Rainforth).

textures can form from a structure that contains shear bands in Mg-RE alloys, but it is also clear that non-RE containing Mg alloys cannot produce the RE texture from a structure containing intensive shear banding [1,10,15,26].

Recently, Stanford et al. [8] reported that recrystallised grains from shear bands tilted away from the extrusion direction gave RE texture orientations. Mackenzie et al. [15] reported the deformed basal texture was replaced by a texture component towards the TD during recrystallisation of a Mg-Zn-Ce alloy. They found many recrystallised grains from shear bands were non-basal and had a growth advantage compared to basal grains during recrystallisation. Basu et al. [4,23] also reported that off-basal grains within shear bands had high mobility relative to basal grains. This mobility difference could be increased when solute drag was taken into account. However, Senn and Agnew [27,28] reported shear bands in a WE53 alloy nucleated grains with a relatively broad spectrum of orientations. A weakened basal texture was produced when the annealing temperature was lower than the precipitation solvus temperature and a random texture was obtained when the annealing temperature was higher than precipitate solvus temperature. Although Senn and Agnew acknowledged that texture evolution may be related to nucleation of specific orientations and preferred grain growth, the mechanism randomising deformed texture was not explicitly explored [27,28]. Their work only provided recrystallisation texture at a single point during partial recrystallisation and after full recrystallisation, and so it was impossible to track grain growth of the recrystallised grains that originated specifically from shear bands. Moreover, the contribution to the final texture from recrystallisation in shear bands could not be differentiated from contributions from other nucleation sites, such as second phase particles, deformation twins, grain boundaries and subgrain boundaries migration [4,8,23,27,28]. It is also still not completely clear whether grain nucleation or grain growth dominates the RE texture evolution during recrystallisation. If the hypothesis that shear band recrystallisation generates the RE texture orientations is true, then there is a major question as to why shear bands in the WE53 alloy, with a relatively large amount of RE additions, did not produce a typical RE texture [27,28]. If the hypothesis is false, then the question arises as to why the RE texture was present in a dilute Mg-RE alloys with shear bands [23,26]?

To address these essential questions, we tracked the entire recrystallisation process from the as-cold rolled state to the fully recrystallisation condition in the WE43 alloy by using a *quasi-in-situ* EBSD method, as presented in Ref. [11]. The mechanical process and heat treatment were purposely adjusted to maximise the production of shear bands in the samples. We have shown that shear bands did not produce the RE orientated grains during nucleation stage. The recrystallised texture was retained during entire recrystallisation process and no preferable grain growth occurred, which is in contrast to the results of other shear band-related recrystallisation texture investigations. The growth advantage of off-basal grains in competition with grains with a basal texture was eliminated by concomitant precipitation. The interactions between shear bands, precipitation, grain growth and recrystallised texture are discussed in detail. Therefore, these findings will inform designing new wrought age hardening Mg alloys and the thermomechanical processes window to improve both strength and formability.

2. Experimental procedure

The WE43 alloy examined is the same as used in our previous work [11,20,29]. A rectangular plate 50 (extrusion direction) $\times$ 25 $\times$ 6 mm^3 was cut from the extruded bar for heat treatment and cold rolling. To restrict significant grain growth after heat

treatment, a short solution treatment was employed. One sample was solution treated for only 10 min at 525 °C (denoted SST10M), followed by cold water quenching. The SST10M sample was then cold rolled with a reduction of 20% in one pass. The solution treatment dissolved the majority of particles, but not all. The effect of these residual particles on recrystallised texture could be ignored due to the limited contribution to the final texture [1,17]. Nevertheless, to explicitly eliminate the effect of residual particles and thereby examine the individual effect of shear bands on recrystallised texture, another sample was produced where all these intermetallic compounds were dissolved. After solution treatment for 4 h, this sample was further subjected to multiple cold rolling (CR) and heat treatment (CR 20% + 525 °C*20mins + CR 20% + 525 °C*10mins) to obtain a similar grain size to that in sample SST10M, but with very limited second phase particles. This sample was denoted as SST4H. The aim of this multiple process was to dissolve the intermetallic particles and refine the grain size as far as possible and therefore more grains could be investigated improving the statistical reliability for the *quasi-in-situ* EBSD. Finally, the SST4H sample was cold rolled with a reduction of 20% in one pass prior to EBSD examination.

The *quasi-in-situ* EBSD sample procedure and scanning experimental details can be found in Refs. [11,20]. The EBSD scans of the same area in sample SST10M were taken after cold rolling and after 300s, 600s, 1020s, 2760s, and 9960s annealing at 490 °C. Similarly, the EBSD scans of sample SST4H were collected after cold rolling and after 285s, 585s, 975s, 1575s, 2775s, and 5175s annealing at 490 °C. In addition, another two recrystallised cold rolled SST4H (one was annealed at 450 °C for 5400s and the other one was annealed at 545 °C for 840s) were also examined by EBSD to explore the effect of annealing temperatures on recrystallised texture. To analyse local misorientation within these microstructure, kernel average misorientation (KAM) maps of the EBSD data were produced using a filter size of 5 $\times$ 5.

3. Results

3.1. Microstructure after solid solution treatment and cold rolling

Fig. 1(a) presents a backscattered SEM micrograph of cold-rolled sample SST4H. The average grain size was calculated to be 35 μm using optical microscopy. Almost all intermetallic compounds formed during casting were dissolved into the Mg matrix except some sparsely distributed RE enriched particles. Hence, the role of particle stimulated recrystallisation on texture evolution can be ignored in this study. Fig. S1(a) (Fig. S1(a) as shown in supplementary material) provides backscattered SEM micrograph of the cold-rolled sample SST10M. A few residual particles were randomly distributed within the sample. Fig. 1(b) gives a large scale EBSD Inverse Pole Figure (IPF) map of the SST4H sample after cold rolling. Shear bands and deformation twins were the two main deformation microstructures observed. The same deformation microstructures were observed in cold-rolled SST10M (Fig. S1(b)). Since most of the sites around the deformation twins were not indexed in the EBSD, it was difficult to determine the specific twin types. A large sampling area was used to track the overall texture evolution during annealing. In addition, to determine the individual contribution to the final recrystallised texture from shear bands and deformation bands, a smaller sampling area was also selected, as shown in Fig. 1(c). Fig. 1(d) is the corresponding KAM map of Fig. 1(c). Fig. 1(e) and Fig. 1(f) are (0002) pole figures of Fig. 1(c) and Fig. 1(b), respectively. Although two EBSD maps had different sampling areas, they both had a similar texture, namely a basal texture with the peak intensity slightly off the basal texture centre. The large EBSD map had a peak intensity of 7.3 multiples of uniform
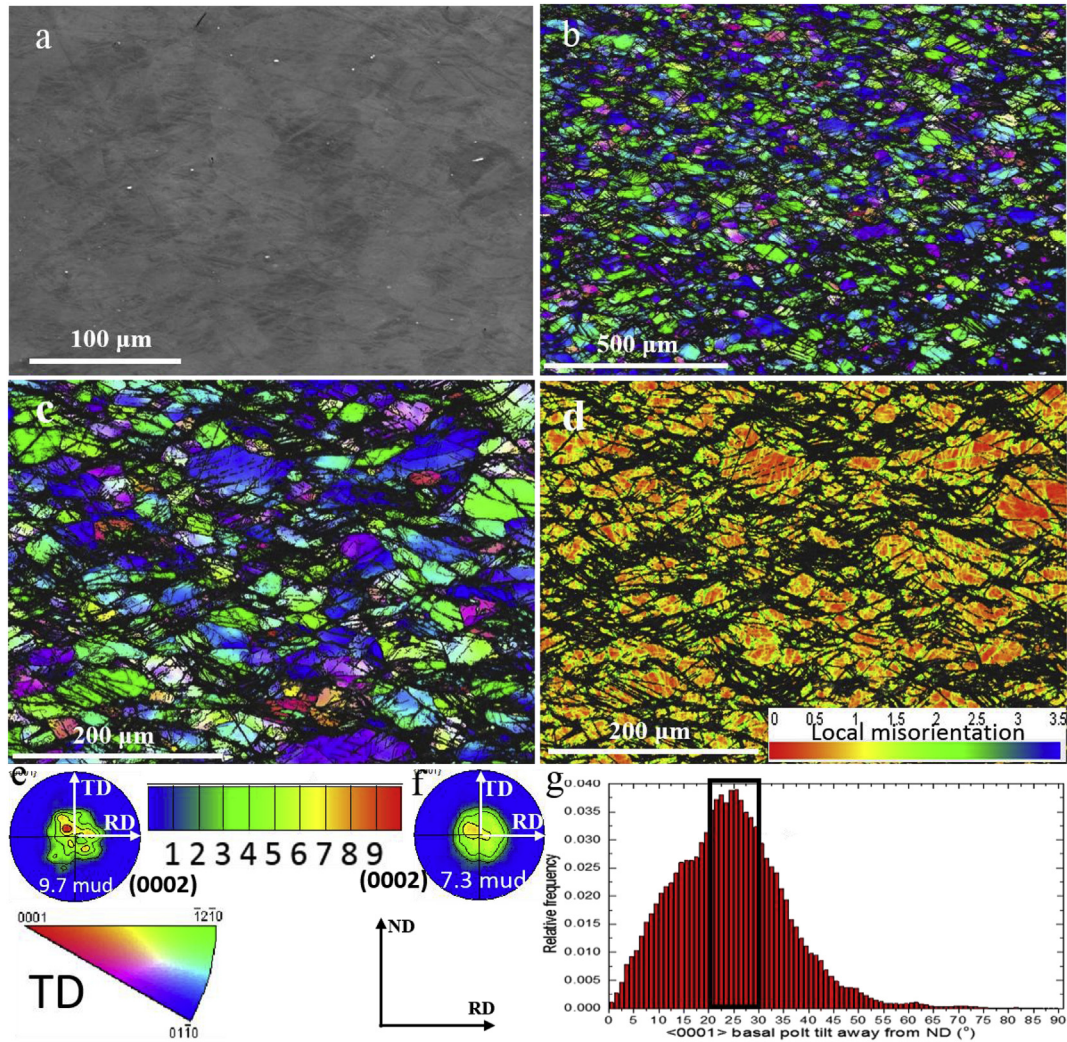
Fig. 1. (a) Backscattered SEM image of cold-rolled sample SST4H, (b) EBSD IPF image of a large area from sample SST4H after cold rolling, (c)) EBSD IPF image of a small area from sample SST4H after cold rolling, (d) corresponding KAM map of (c) showing the stored energy distribution (the non-indexed areas have the highest local strain). (e) (0002) pole figure of (c), and (f) (0002) pole figure of (b). (g) distribution of <0001> direction corresponding to each grain orientation in (b). Observation along TD was applied to IPF triangle.

density (mud) while the small EBSD map had a peak intensity of 9.7 mud. Fig. 1(g) shows the distribution of the <0001> direction corresponding to each grain orientation in Fig. 1(b) after cold rolling. It shows a peak at 20–30° tilted away from the ND and most texture components are distributed within 0–45°, which is consistent with pole figure result presented in Fig. 1(f).

3.2. Grain nucleation and growth from shear bands and deformation twins

Fig. 2(a–f) presents the entire recrystallisation process from nucleation to full recrystallisation of the same sampling area in Fig. 1(c), which allows the origin of the recrystallised grains to be determined as well as following their subsequent growth. After 285s annealing, Fig. 2(a), small recrystallised grains appeared within the shear bands and at deformation twins. The recrystallised grains originating from deformation twins were marked by the circles and ovals in Fig. 2. The deformation twin density was lower in sample SST4H with an average grain size of 35 μm than the sample SST1H studied in our previous work [20]. Fig. 2(b–f) show that many of these recrystallised grains that formed in deformation twins were subsequently consumed by recrystallised grains

generated from shear bands. Because the density of the twins was low and the number of double twin intersections was particularly low (Fig. 1(c)), recrystallised grains from double twins could not grow out of twin boundaries easily to consume adjacent parent grains. Therefore, it is not surprising that recrystallised grains from shear bands, which occupied a much higher volume fraction, consumed constrained recrystallised grains from double twins during recrystallisation. The recrystallised volume fraction contributed by deformation twins was measured to be only ~5.6% after nearly full recrystallisation. To further validate the reliability of the results, recrystallised grains from deformation twins in cold-rolled SST10M were also tracked by *quasi-in-situ* EBSD and the final recrystallised volume fraction contributed by deformation twins was measured to be only ~4%, Fig. S2. Hence, the effect of deformation twins on recrystallised texture evolution was small and the main contribution to the recrystallised texture came from recrystallisation in the shear bands in this sample.

The magnification in Fig. 2 is too small to distinguish deformed grain boundary and subgrain boundary recrystallisation due to boundary migration from shear band recrystallisation. Therefore, representative high magnification images from samples SST10M and SST4H are provided in Fig. 3 and Fig. 4, respectively. The small
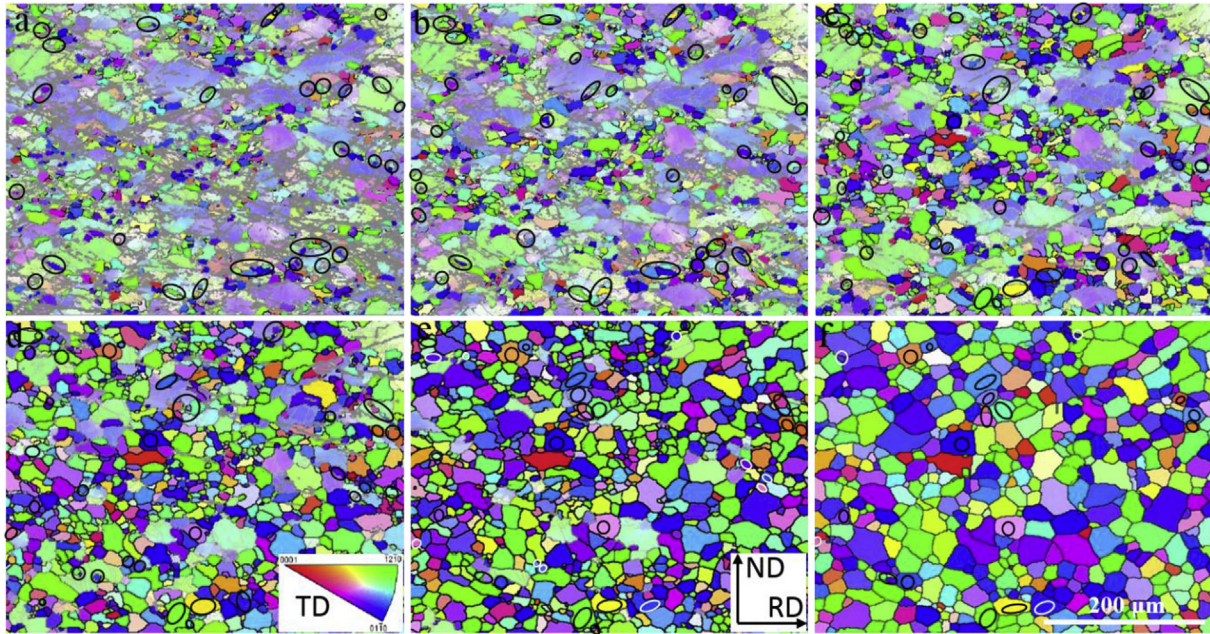
Fig. 2. (a) EBSD IPF maps of cold-rolled sample SST4H only showing recrystallised at annealing intervals of (a) 285s, (b) 585s, (c) 975s, (d) 1575s, (e) 2775s and (f) 5175s. The recrystallised grains originating from deformation twins were marked by the circles and ovals. Observation along TD was applied to IPF triangle.
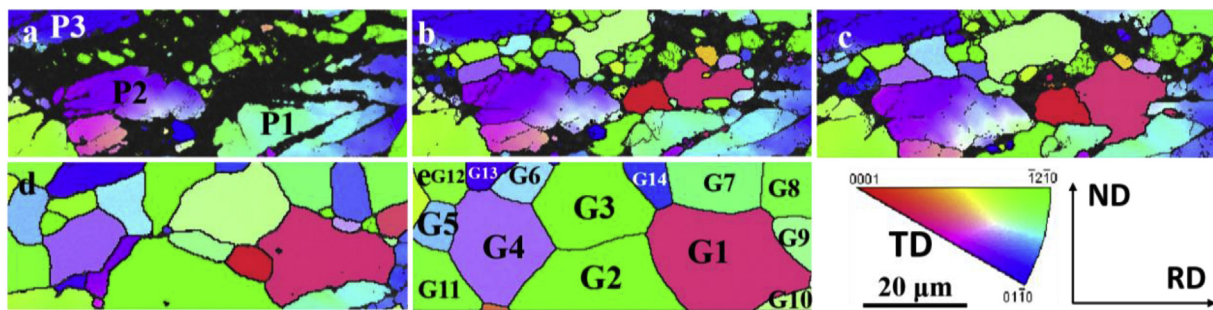

Fig. 3. *Quasi-in-situ* EBSD IPF maps presenting recrystallised grain nucleation and growth in sample SST10M (a) cold-rolled and at annealing intervals of (b) 300s, (c) 600s, (d) 1020s and (e) 2760s. Observation along TD was applied to IPF triangle.

area in Fig. 3(a) from sample SST10M contains three deformed parent grains (P1, P2 and P3) and intense shear bands. After annealing for 300s (Fig. 3(b)) and 600s (Fig. 3(c)), all recrystallised grains nucleated from shear bands expanded into the adjacent P1 and P2 grains. In addition, a deformed twin in grain P1 was consumed by grain G1 during recrystallisation. After annealing 1020s and 2760s, small recrystallised grains were gradually consumed by larger recrystallised grains originating from shear bands, as shown in Fig. 3(e). More specifically, grains G1-G7 were originally from shear bands within grains P1 and P2, and grains G8-G14 were from shear bands in adjacent areas. Another small area from sample SST4H in Fig. 4 presents the recrystallisation processes including nucleation and growth. Again, shear bands were preferable nucleation sites and most of the grains consumed deformed parent grains and small recrystallised grains (Fig. 4(a–f)). However, some recrystallised grains nucleated at high angle grain boundaries between a recrystallised grain and residual deformed parent grain. As shown in Fig. 4(g), which uses the same EBSD data of Figs. 4(f) and 6 grains (e.g., G1, G2, G4, G5, G6, G8) in Fig. 4(g) nucleated from grain boundaries instead of within shear bands. Most of these type of grains appeared in the late stage of the recrystallisation process (e.g., after annealing 2775s) and some of them were

consumed by adjacent recrystallised grains after further annealing due to small grain size (e.g., a green grain G9 in Fig. 4(e)). Another two grains marked G3 and G7 in Fig. 4 (g) could have come from the grains beneath this 2-D surface due to 3-D grain growth.

In addition, grains arising from both continuous and discontinuous subgrain growth need to be considered and normally have the orientation of the host deformed parent grain [23,30,31]. However, by carefully comparing the orientations of the recrystallised grains and deformed parent grains, it was clear that no recrystallised grains had similar orientations to that of the deformed parent grains. Therefore, if recrystallisation by subgrain growth occurred, it was minimal and did not contribute to the final texture.

The volume fraction of the 8 grains in Fig. 4(g) that arose from recrystallisation at high angle grain boundaries was 9.7%. Fig. 4(h) plots corresponding (0002) pole figure of these 8 grains and indicates these grains were distributed randomly. To find out the influence of grain boundary recrystallisation on texture evolution, Fig. 4(i) plots (0002) pole figure of the recrystallised grains that were known to have originated from shear bands (semi-transparent grains in Fig. 4(g)) and Fig. 4(i) gives (0002) pole figure of all recrystallised grains in Fig. 4(g). Comparing these two pole figures
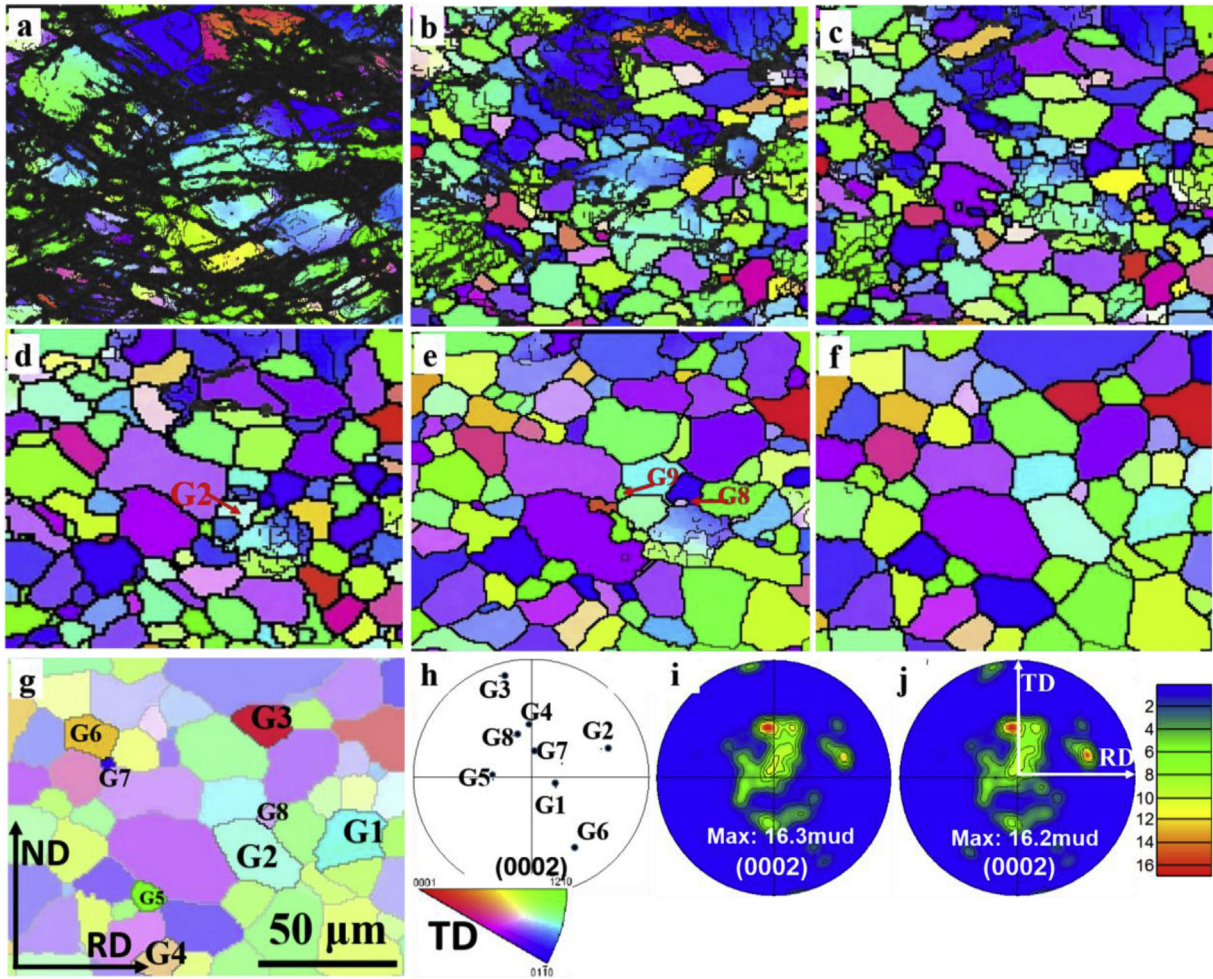
Fig. 4. *Quasi-in-situ* EBSD IPF maps presenting recrystallised grain nucleation and growth in sample SST4H (a) cold-rolled, and at annealing intervals of (b) 585s, (c) 975s, (d) 1575s, (e) 2775s and (f) 5175s. (g) Highlighted grains were nucleated by grain boundary nucleation in late recrystallisation stage in (f). (h) (0002) scattered data pole figure of (g), (i) (0002) pole figure of grains by shear bands recrystallisation and (j) (0002) pole figure of all grains in (g). Observation along TD was applied to IPF triangle.

it is clear that the grain boundary recrystallisation occurred in the late stage of recrystallisation and did not change the recrystallised texture distributions or intensity significantly. Another set of quasi-is-situ EBSD data from sample SST4H was provided in Fig. S3. The volume fraction of grain boundary recrystallised grains was calculated to be 14.2%. The recrystallised grains G1-G5 (Fig. S3) again had random orientations. Although the texture intensity from only shear band recrystallisation and from all grains was different, the texture distributions were quite similar.

Based on the aforementioned results, the effect of deformation twins, grain and subgrain boundary, second phase particles recrystallisation on texture evolution was not significant. Therefore, the texture evolution in this sample can be largely attributed to shear band recrystallisation. Another large area EBSD scan (Fig. 1(b)) was used to statistically investigate the effect of shear bands on texture evolution during the entire recrystallisation process from nucleation to full recrystallisation. Fig. 5(a−f) give the entire recrystallisation process from nucleation to complete recrystallisation of the same large scanning EBSD area of Fig. 1(b). After 285s annealing, Fig. 5(a), small recrystallised grains were detected, heterogeneously distributed within the original shear band directions, which were tilted ±30−50° from rolling direction (two sets of representative recrystallised grain bands are marked in Fig. 5(a)). This again confirmed that recrystallisation was

principally nucleated in the shear bands. After 585s and 975s annealing, the recrystallised grains started to grow and more recrystallised grains appeared in the shear bands. Subsequently, recrystallised grain growth, rather than the formation of new recrystallised grains, dominated the recrystallisation process. Recrystallised grains expanded into adjacent deformed parent grains and consumed smaller recrystallised grains during grain growth between 1575s and 5175s annealing.

Fig. 6 shows the total recrystallised volume fraction (V_t) of the cold-rolled sample SST4H as a function of annealing time. After 285s, the recrystallised volume fraction was 23.0%, which was much faster than sample SST1H, reported in Ref. [20] and SST24H, reported in Ref. [11]. Subsequently, the recrystallised volume fraction, V_t, increased after 585s 30.6%. The value of V_t was determined by the recrystallised grains consuming the surrounding as-deformed matrix and larger recrystallised grains consuming smaller ones, leading to a V_t of 54.7% and 76.0% after annealing 975s and 1575s, respectively. Finally values of V_t of 93.4% and 98.8% were measured after annealing 2775s and 5175s.

3.3. Texture evolution of all recrystallised grains during annealing

(0002) pole figures, collected from only recrystallised grains (Fig. 5), are given in Fig. 7(a−f). Fig. 7(a) gives a pole figure after
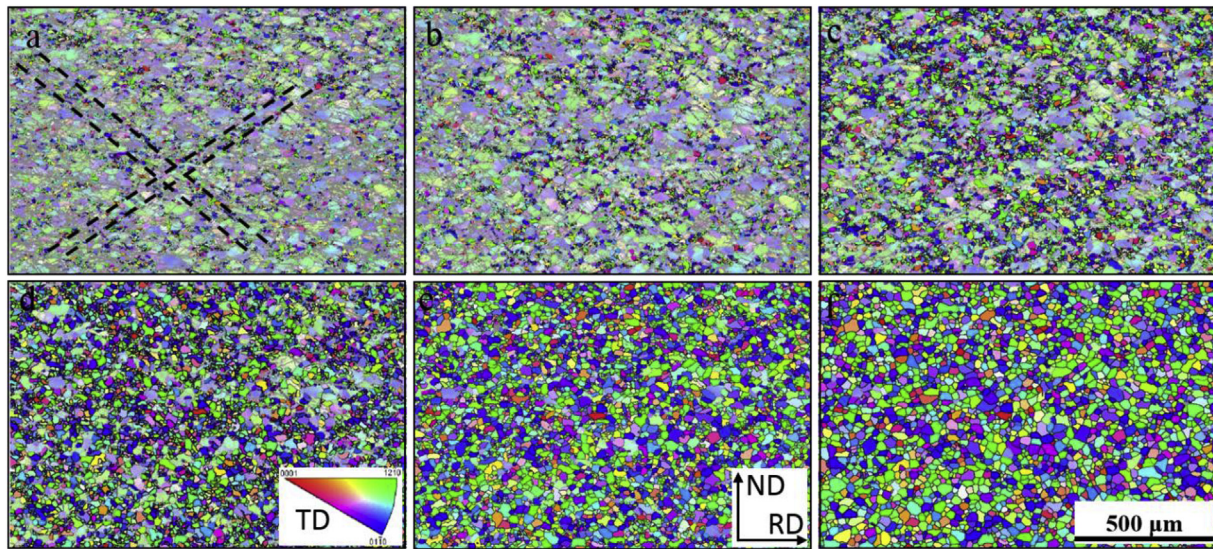
Fig. 5. EBSD IPF subset maps only showing recrystallised grains mainly around shear bands at annealing intervals of (a) 285s, (b) 585s, (c) 975s, (d) 1575s, (e) 2775s and (f) 5175s. The axes system is the same as shown in Fig. 3(e). Observation along TD was applied to IPF triangle.
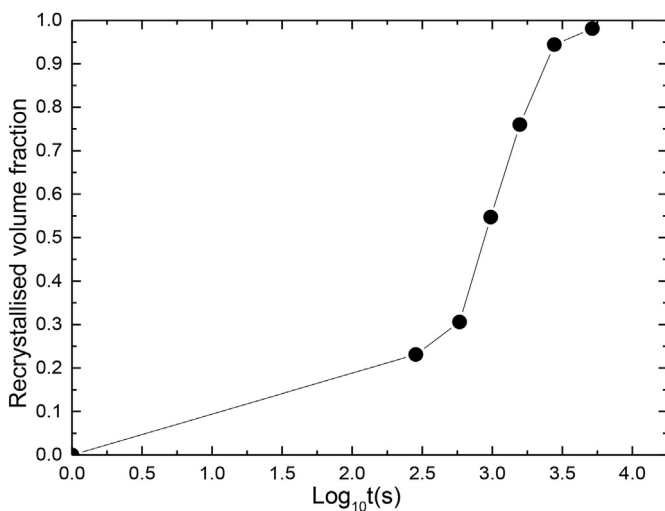

Fig. 6. Recrystallised volume fraction as function of annealing time of cold-rolled sample SST4H.

285s annealing at which time substantial nucleation of recrystallised grains took place. Overall, the pole figure (Fig. 7(a)) shows a weakened basal texture with a peak intensity of 5.2 mud compared to the deformed texture (Fig. 1(f)) of 7.7. No evidence of a RE texture was observed. Nonetheless, other relative weak texture components were scattered between RD and TD directions. With further annealing, although the texture distribution varied slightly (Fig. 7(b—f)), the weakened basal texture and the peak intensity were retained during the entire recrystallisation process.

3.4. Evolution of individual texture components during annealing

Fig. 8 plots the distribution of <0001> direction corresponding to each grain orientation. It was obvious that the texture component distribution was well preserved during the whole recrystallisation process except some spikes (e.g., a spike at 20° in Fig. 8(c)), which was consistent with the (0002) pole figure results (Fig. 7). Compared to the distribution of the <0001> direction in the cold-

rolled sample (Fig. 1(g)), the texture component distributed in the range of 70—90° can be clearly seen and the peak texture component shifted, being tilted 25—37.5° away from the ND after annealing. Moreover, the peak relative frequency decreased from approximately 0.039 in cold-rolled state to 0.028 after various annealing intervals. This indicated both texture position and intensity were changed by the recrystallisation.

To determine whether some grains grew favourably during annealing, the recrystallised grains were divided into four groups as designated in our previous paper [20]. These four groups were 0—20° (TCA), 20—45°(TCB), 45—70°(TCC) and 70—90°(TCD) tilted away from the ND.

Figs. S4-S7 presents a sequence of EBSD IPF subset maps of TCA, TCB, TCC and TCD grains from SST4H (Fig. 5). The insets in Figs. S4—S7 are corresponding (0002) pole figures. For grains with TCA orientations, grains were orientated relatively homogeneously within the region of 0—20° tilted away from the ND and the peak texture intensity fluctuated around 23 mud (Fig. S4). For grains with TCB orientations, grains were uniformly distributed between TD and RD directions with peak texture intensity around 6.5 from 285s to 1575s. With further annealing, some texture components between RD and TD were slightly intensified (Figs. S5(e—f)). Fig. S6 shows grains with the TCC orientation. These grains had a similar texture evolution to the TCB grains. For TCD grains (Fig. S7), the position of peak intensity was gradually transferred from lower to upper hemisphere, but the number of grains within this texture component was not high.

During the past decade, oriented grain growth of recrystallised grains in shear bands has been reported arising from solute drag or Zener pinning [4,21,23], which is believed to be the main mechanisms driving the formation of the RE texture. To investigate this, Fig. 9 plots the mean grain size of recrystallised grains of each texture component. The average grain size of each texture component was nearly all the same from nucleation to full recrystallisation. This indicated there was no orientated grain growth occurred during annealing. Fig. 8(a) plots the recrystallised grain number collected from each texture component. TCB exhibited the most grains throughout the entire recrystallisation process, followed by TCA, TCC and TCD. The grain number peaked after 975s annealing when the nucleation sites were saturated and
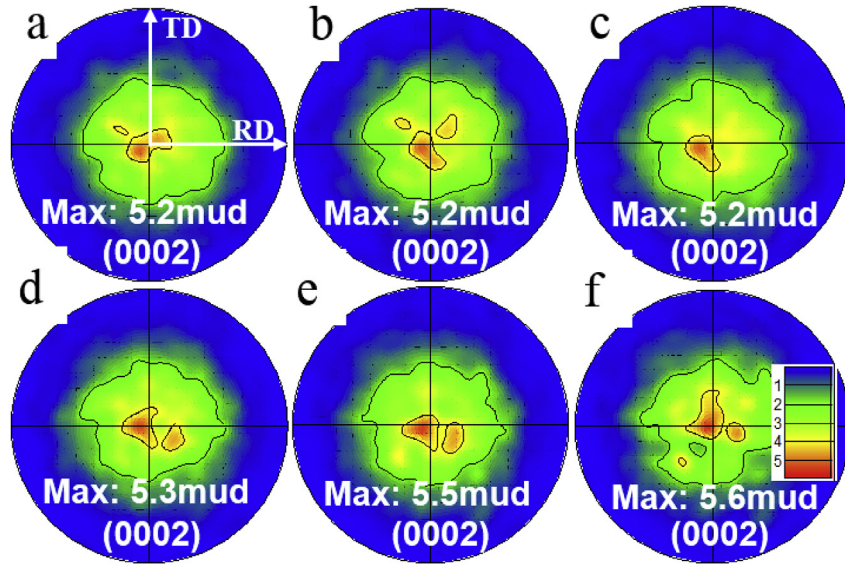
Fig. 7. (0002) pole figures consisting only of recrystallised grains mainly formed at shear bands at annealing intervals of (a) 285s, (b) 585s, (c) 975s, (d) 1575s, (e) 2775s and (f) 5175s. The axes systems are all the same as shown in Fig. 5(a) and legend is shown in Fig. 6(f).
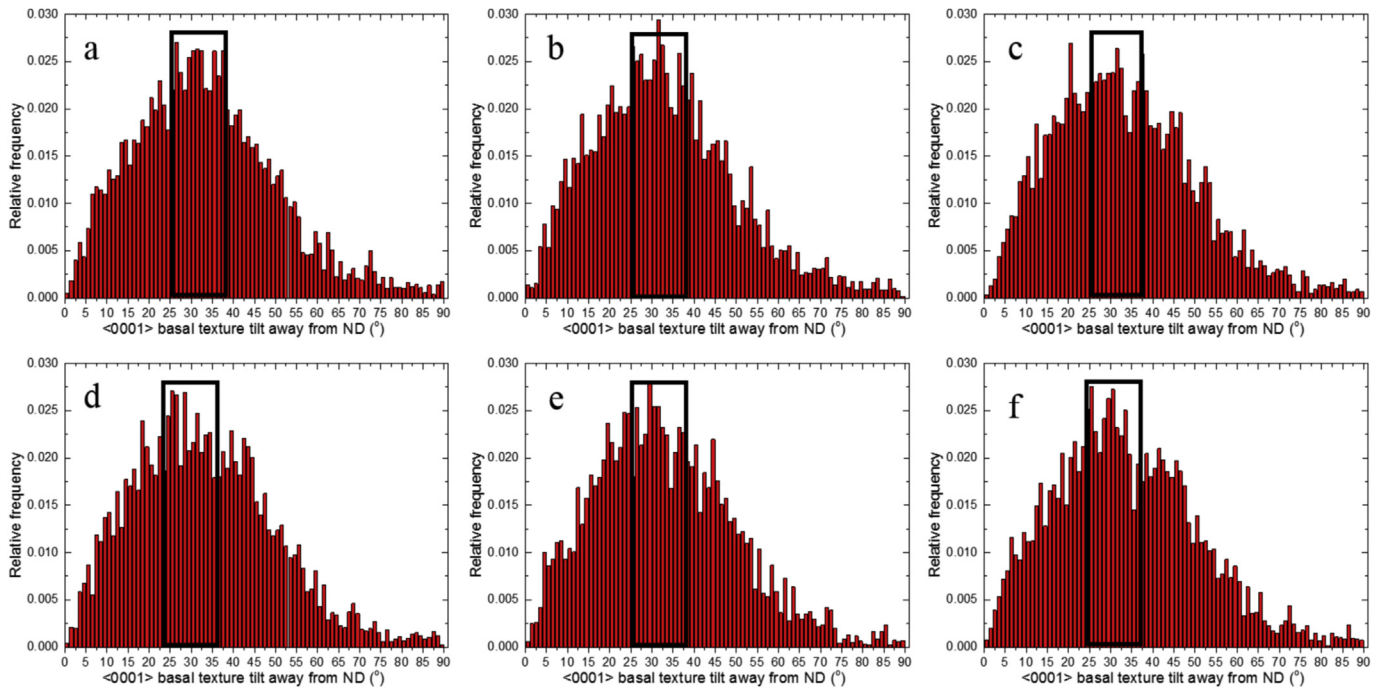

Fig. 8. <0001> basal texture tilted away from Normal Direction (ND) at annealing intervals of (a) 285s, (b) 585s, (c) 975s, (d) 1575s, (e) 2775s and (f) 5175s.

decreased thereafter (Figs. 5—7). The grain number fraction of recrystallised grains of an individual texture component based on the total recrystallised grain number after each annealing interval is given in Fig. 10(b). The recrystallised grain number fraction of each texture component was not changed significantly over the entire annealing process. Thus, mutual grain consumption during the grain impinging stage was equal across all orientations.

Fig. 11 plots the volume fraction of each texture component based on total recrystallised area, excluding the residual un-recrystallised area. Although there were substantial differences in the recrystallised volume fractions from each component, the volume fraction of each texture component was well maintained during recrystallised grain growth, which is consistent with the results presented in Fig. 10(b). This resulted from the uniform grain growth during recrystallisation (Fig. 9). Since the average grain size of each texture component was very close, it was not surprising to find the data from Fig. 10(b) and Fig. 11 were nearly the same. The TCB recrystallised had the largest fraction (Fig. 11), which was a result of recrystallised grains having this orientation formed at the nucleation stage (Fig. 10) which was unchanged by subsequent uniform grain growth (Fig. 9).
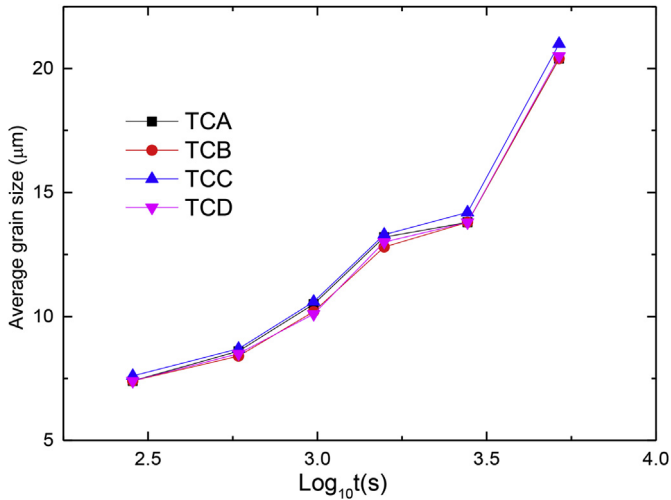
Fig. 9. Average grain size of each recrystallised texture component as a function of annealing time.

Fig. 11. Recrystallised volume fraction of each texture component based only on the recrystallised area as a function of annealing time.

3.5. Precipitation during recrystallisation

As mentioned in previous studies [20,29], recrystallisation was accompanied by a concomitant precipitation and re-dissolution process in this alloy. Fig. 12 provides a series of backscattered SEM micrographs to show the evolution of precipitation. After 285s annealing at 490 °C, fine precipitates started to appear, especially along grain boundaries and twin boundaries (Fig. 1(a)). After 585s annealing, precipitate coarsening also took place (Fig. 12(b)). Fig. 12(c) shows that these precipitates could still be observed along the prior boundaries after annealing 975s, but the size of these precipitates was reduced due to re-dissolution during recrystallisation. After annealing 5175s, the precipitates completely re-dissolved into the matrix (Fig. 12(d)). The entire precipitation and re-dissolution process was illustrated in detail elsewhere recently by using *in-situ* TEM [29].

3.6. Recrystallised textures after annealing at various temperatures

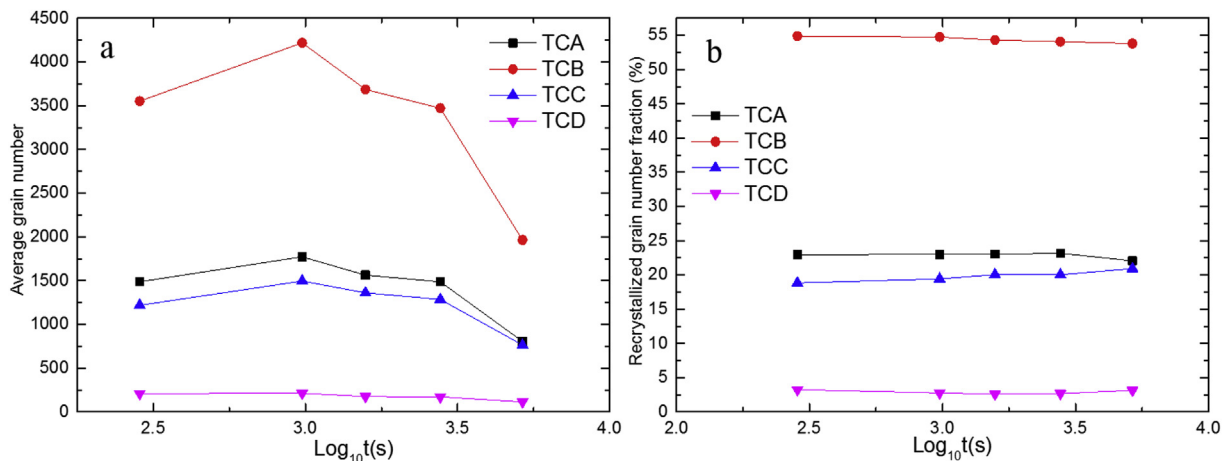To find out the effect of annealing temperature on recrystallised texture, samples annealed at 400 °C, 450 °C, 490 °C and 545 °C were investigated and compared (three temperatures were below and one temperature was above solvus temperature of 525 °C). After annealing at 400 °C for 5400s, significant precipitation occurred but was associated with negligible recrystallisation (which was not presented here). Fig. 13 (a,g,m) provide EBSD IPF maps of samples after annealing 5400 s at 450 °C, 5875 s at 490 °C and 840 s at 545 °C. The recrystallised grains in these three maps were divided into two groups. The grain size of highlighted small grains was below average grain size while the grain size of the semi-transparent larger grains was above the average grain size. The mean grain sizes were approximately 19.0 μm, 20.5 μm and 56.0 μm in Fig. 13(a), Fig. 13(g) and Fig. 13(m), respectively. Fig. 13(b−d) give the recrystallised texture of grains below and above the average and the whole data set after annealing at 450 °C for 5400s. Although the texture shape was different between smaller and larger grains, both can be defined as a weakened basal texture with scattered relative weak off-basal texture components. The texture component distribution with respect to the <0001> basal poles tilting away from the ND were very similar when small grains (Fig. 13(e)) were compared to larger grains (Fig. 13(f)). Both pole figures and texture component distributions results indicated that

Fig. 10. (a) Recrystallised grain number of each texture component and (b) recrystallised grain number fraction of each texture component based on the whole recrystallised grain number as a function of annealing time.
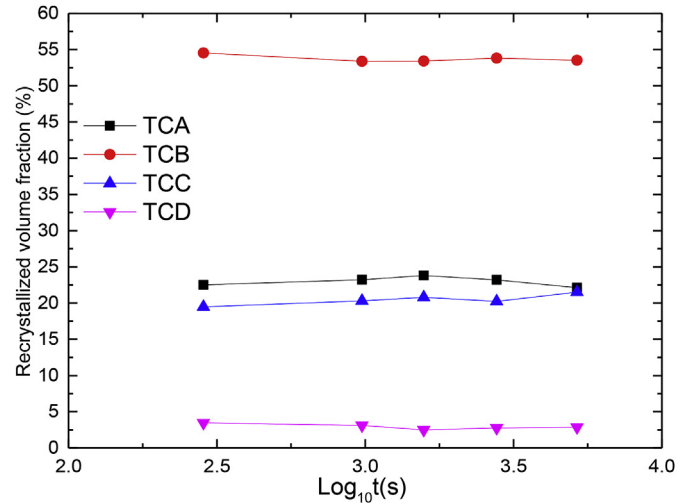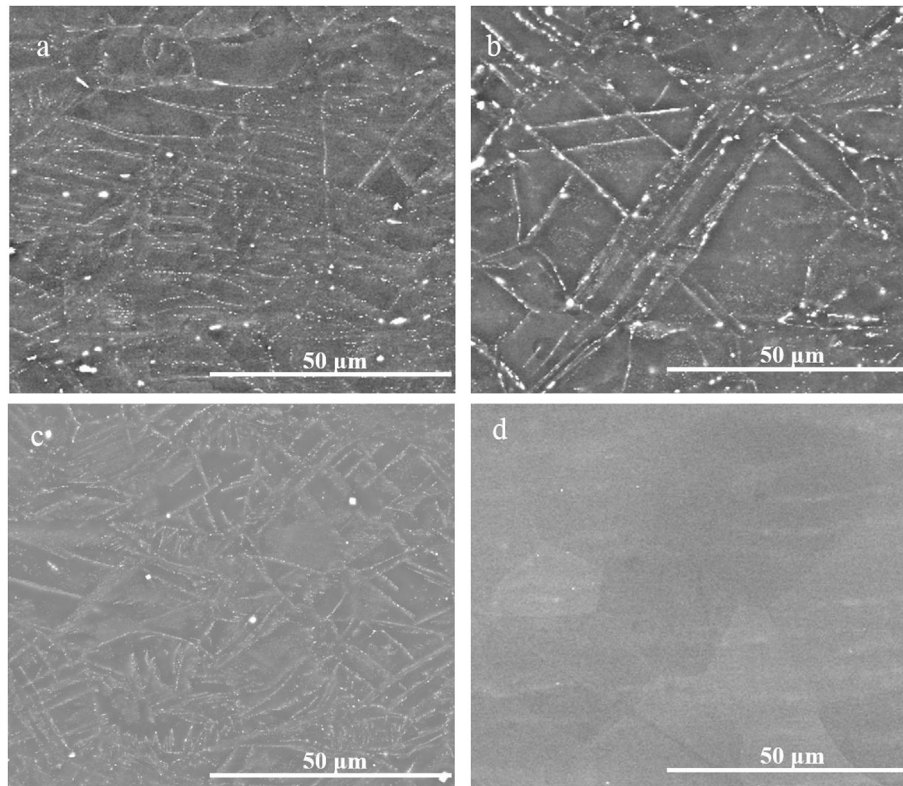
Fig. 12. Backscattered SEM images after annealing (a) 285s, (b) 585s, (c) 975s and (d) 5175 s at 490 °C.

there was no preferable grain growth of some specific orientations. Otherwise, the texture component distributions would be significantly different in Fig. 13(e) and Fig. 13(f).

After annealing at 490 °C for 5875s (Fig. 13(g)), similar results were obtained as described in sample after annealing at 450 °C. A weakened basal texture with scattered relative weak off-basal texture components was found in Fig. 13(h) and Fig. 13(i). There was no noteworthy difference regarding texture component distributions between small and larger grain areas, Fig. 13(k) and Fig. 13(l). In other words, texture component evolution followed the same trend with various grain sizes and no orientated growth took place.

However, when the sample was annealed at 545 °C, above precipitate solvus temperature, for only 840s, the recrystallised texture from small grains were quite different from the larger grains. Fig. 13(n) shows a (0002) pole figure of the smaller grains which exhibited a diffuse basal texture. Fig. 13(o) presents the recrystallised texture contributed by the larger grains tilted towards the TD direction. The texture component had a high frequency of basal poles tilted away from the ND below 20° in smaller grains (Fig. 13(q)). In contrast, the peak frequencies ranged around 30—45° in larger grains (Fig. 13(r)). Hence, orientated growth occurred after annealing at 545 °C: grains with off-basal orientations had a growth advantage compared to grains with basal orientations. Equally, the recrystallised texture from all recrystallised grains after annealing at 545 °C tilted towards the TD with weak scattered texture components (Fig. 13(p)), which was changed considerably relative to whole recrystallised grains texture when the sample was annealed at 450 °C (Fig. 13(d)) and 490 °C (Fig. 13(j)).

4. Discussion

4.1. Effect of concurrent precipitation during early recrystallisation process

The grain boundaries were not found to be active nucleation sites in the early stage of recrystallisation process, especially during nucleation stage. The detailed mechanism of the retardation of recrystallisation along prior grain boundaries has been demonstrated recently and so will not be described in detail here [20]. Briefly, concomitant precipitation on the grain boundaries during annealing exerted strong Zener pinning that inhibited grain boundary movement and hence recrystallisation through the prevention of strain induced boundary movement (SIBM) [32]. Precipitates can clearly be seen distributed along grain and deformation twin boundaries (Fig. 12(a−c)). This is an important point as recrystallisation arising from SIBM results in a basal texture and therefore it is key to generate weaker, more uniform, textures that the grain boundaries are pinned. Clearly, precipitation on grain boundaries is beneficial to the formation of a weakened basal texture.

Although the stored energy in shear bands was much higher than at prior grain boundaries, the effect of Zener pinning on shear band recrystallisation needs to be estimated as it cannot be accurately calculated during the early stages of annealing. The driving force (P_d) from shear bands, Zener pinning force from concurrent precipitation (P_z) and retarding pressure due to boundary curvature (P_c) were approximately calculated [31]. Image J was used to calculate the local volume fraction of second phase particles and average radius. All the parameters are listed in Table S1.
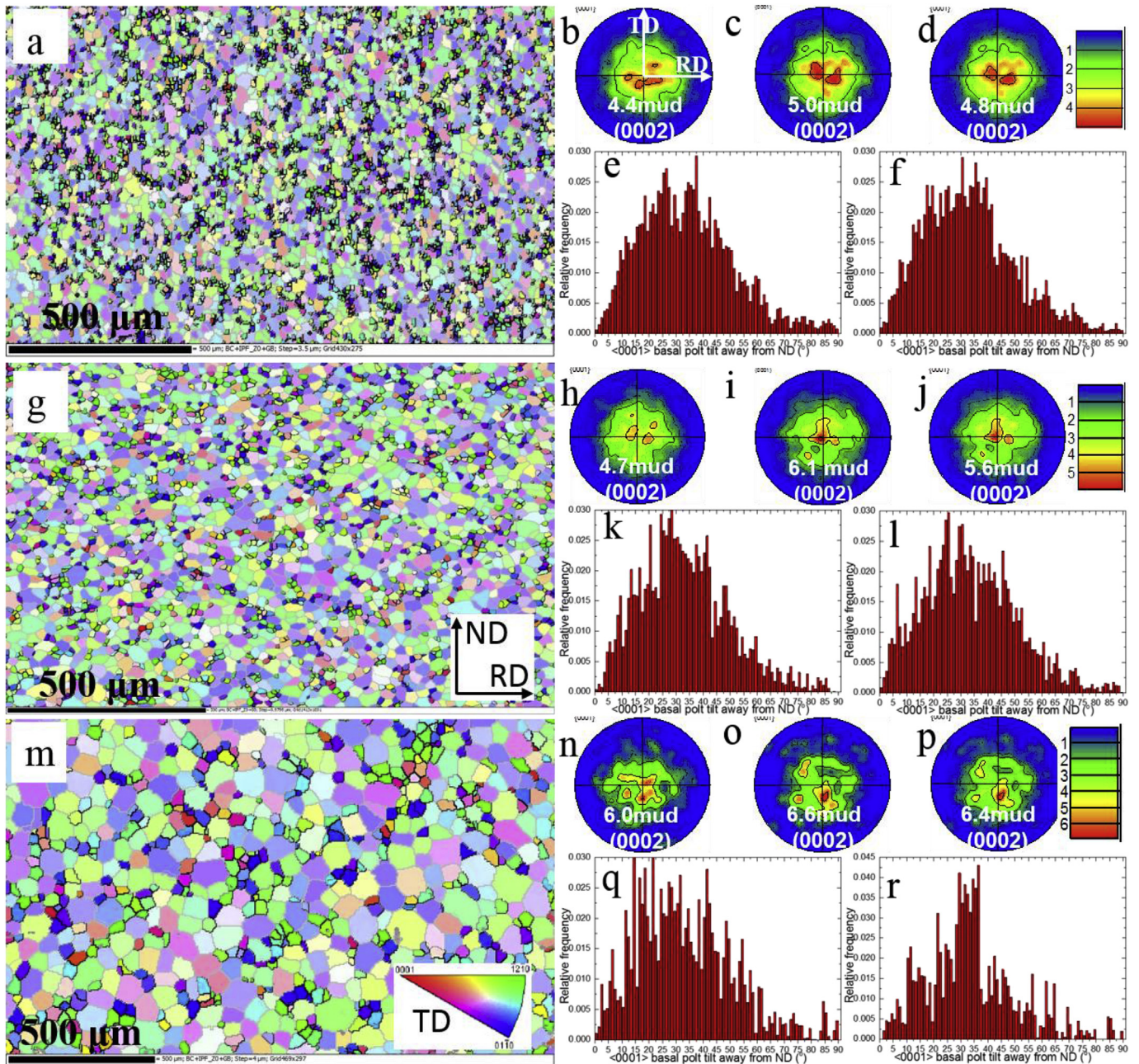
Fig. 13. EBSD IPF map of cold-rolled sample SST4H annealing at (a) 450 °C for 5400s, (g) 490 °C for 5175s and (m) 545 °C for 840s (highlighted grains were smaller than while semi-transparent grains were larger than the average grains size). (b–d) (0002) pole figures of smaller grains, larger grains and all grains from (a). (e–f) <0001> basal texture tilted away from the ND collected from smaller and larger grains from (a). (h–j) (0002) pole figures of smaller grains, larger grains and all grains from (g). (k–l) <0001> basal texture tilted away from the ND collected from smaller and bigger grains from (g). (n–p) (0002) pole figures of smaller grains, larger grains and all grains from (m). (q–r) <0001> basal texture tilted away ND collected from smaller and bigger grains from (m). The axes systems of pole figures are all the same as shown in Fig. 11(b). Observation along TD was applied to IPF triangle.

$$P_d = \alpha \rho G b^2 \tag{1}$$

$$P_z = \frac{3F_v\gamma}{2r} \tag{2}$$

$$P_c = \frac{2\gamma}{R} \tag{3}$$

where α is a constant of ~0.5, typical average dislocation density ρ was estimated to be $10^{15} \mathrm{m}^{-2}$, G of Mg is 12.7 GPa, b is 0.32 nm [33],

γ is high grain boundary energy of ~0.4J/m^2 [34], Fv is local volume fraction of second phase particles, r is the average radius of these particles and R is the average size of recrystallised grains. Dislocation density was not uniformly distributed due to the heterogeneously deformed microstructure. It can be expected that dislocation density in shear bands should be much higher than average due to large orientation gradient within shear bands compare to adjacent deformed grains. However, to simplify this calculation, the estimated average dislocation density of 10^{15} m^{-2} was used to evaluate the as-deformed shear band recrystallisation behaviour during the early stage of annealing. Furthermore, solute

drag was not considered because the sample was annealed at a high temperature close to the solvus temperature and the concurrent precipitation would have reduced the extent of segregated solute.

Although the stored energy was used in calculation was certainly an underestimate, Table S1 shows that P_d was at least two times of $P_z + P_c$ after annealing 285s, 585s and 975s. Therefore, this suggests that the recrystallised grain growth was only slowed but not stagnated by concurrent precipitation in the early stage of recrystallisation. In addition, at the onset of recrystallisation (e.g., only after annealing 10s), the high stored energy in the shear bands and the small volume fraction of precipitates would mean that the precipitation would not have inhibited recrystallisation within the shear bands.

4.2. Mechanism of recrystallised grain growth and texture evolution during annealing

The typical RE texture formed in Mg-RE alloys with shear bands [4,8,15,23,26] was not produced in this work, where the material was processed to contain intensive shear bands. This was true both during nucleation or subsequent growth of the recrystallised grains (Fig. 7). A weakened basal texture with relative weak scattered texture components between RD and ND directions was generated during the nucleation stage. This type of recrystallised texture was retained during the entire subsequent grain growth and the peak texture intensity strengthened only slightly in the later stage of grain growth. The question, therefore, is how this weakened basal texture appeared and was preserved throughout the entire recrystallisation process.

4.2.1. Formation of recrystallised texture at nucleation

Prior grain and subgrain boundaries, deformation twins, shear bands and second phase particles were considered as the main nucleation sites for recrystallisation in Mg alloys [1,10]. In this study, the effect of nucleation of recrystallisation at deformation twins and initial second phase particles does not need to be considered due to low volume fraction, which made their contribution to the final texture negligible (Fig. 1(a), Fig. 2 and Fig. S2). The majority of recrystallisation occurred at shear bands (Figs. 2–5, Figs. S2–3). Concurrent precipitation occurred during recrystallisation and the size of some particles after coarsening was larger than 1 μm. Deformation zones formed at large particles are prerequisites for particle stimulated nucleation (PSN) of recrystallisation. However, in the current work there were no deformation zones associated with these particles and so PSN was not considered to occur in this case. Grain boundaries were not active nucleation sites at the early stage of recrystallisation and no clear evidence of recrystallisation by subgrain boundary migration was found during the entire recrystallisation process (Figs. 3–4 and Fig. S3). Therefore, recrystallisation at the shear bands were the main source of recrystallised texture at nucleation stage. A wide spectrum of orientations can be generated during recrystallisation in shear bands due to the existence of a wide range of internal misorientations. In Mg alloys, previous work showed the recrystallised grains nucleated within shear bands had randomised orientations [4,8,15,21,23]. After 285s annealing at 490 °C, the nucleation of recrystallised grains within shear bands did not produce a specific texture component (e.g., RE texture), but a relatively randomised texture (Fig. 7(a)) with a weakened basal texture and scattered texture components. This was a result of a wide range of local misorientation within shear bands nucleating randomly oriented recrystallised grains, in agreement with published results [4,8,15,21,23].

4.2.2. Mechanism of grain growth and texture evolution controlled by simultaneous precipitation and re-dissolution

The final recrystallised texture either depends on the nucleation of oriented grains or the subsequent favourable growth of specific orientations or both [1,10,28]. Orientated grain growth has been observed in other Mg-RE alloys that contained shear bands [4,8,15,23,26]. In the current work, no preferential grain growth was observed, such that the texture formed at the nucleation stage was stable and growth rates were equivalent for all orientations throughout subsequent grain growth.

Most research work related to shear band recrystallisation suggested solute drag played a critical role in texture evolution [4,8,15,23]. Solute drag caused by segregation along recrystallised grain boundaries increased the grain boundary mobility difference between the slow basal and the quicker off-basal grains. Therefore, off-basal grains had a growth advantage over basal grains when they consumed deformed grains.

However as shown in Fig. 7, there was no evidence of a RE texture throughout annealing. The main difference between the current study and other research where a RE texture was observed, was the simultaneous precipitation and re-dissolution on grain and twin boundaries of second phase particles that we found during recrystallisation, Fig. 12. The difference could be attributed to a higher amount of RE additions (7 wt%) in the current alloy compared to ~1 wt% in the alloy studied by Refs. [4,8,15,23,35]. These precipitates (Fig. 12(a–c)) exerted Zener pinning to suppress grain growth. Precipitation is known to have a significant effect on texture evolution. For example, Basu et al. observed a strong basal texture in a Mg-1Ce alloy after annealing [4]. Uniformly distributed $Mg_{12}Ce$ precipitates hindered any orientated growth resulting in the basal texture [4,23]. In addition, pre-existing string-like second phase particles or intergranular precipitation stimulated by significant segregation along grain boundaries reduced the effective role of RE solute and the growth of grains with specific orientations [1,35,36]. In the current work, and the accompanying paper [20], it was the concurrent precipitation of second phase particles during recrystallisation that restricted any potential preferential grain growth and allowed for uniform grain growth among all texture components (Figs. 9–11). Although grain boundary recrystallisation occurred during the late stage of recrystallisation (Fig. 3 and Fig. S3) when the precipitates started to re-dissolve into matrix, recrystallised grains from grain boundaries was only a small fraction (approximately 10%) and these grains had random orientations, and so did not change the dominant role of shear band recrystallisation on texture evolution. These are the main reasons why the recrystallised texture morphology at the nucleation stage was well maintained during the entire recrystallisation process and was not turned into an RE texture which has been widely reported in Mg-RE alloys with significant shear band recrystallisation [4,8,15,23].

Grain boundary recrystallisation was found to be at the high angle grain boundary between a recrystallised grain and a residual deformed grain, instead of from original deformed grain boundary between two deformed parent grains. One reason for the limited recrystallisation from the original grain boundaries was that they were pinned by concurrent precipitation at the early part of recrystallisation and subsequently most of them were consumed by adjacent recrystallised grains by shear band recrystallisation.

4.2.3. Effect of annealing temperature on texture evolution

The annealing temperature (below/above the particle solvus temperature) had a significant effect on the recrystallisation texture (Fig. 13) with the mechanism being a function of temperature. The various textures obtained above and below the solvus temperature have also previously been reported in a WE53 alloy, but there was

no detailed analysis of the mechanism [27,28]. A schematic presented in Ref. [20] has been slightly modified based on the recrystallised temperatures used in this work (Fig. 14). Points A and B shown in Fig. 14 are precipitation and recrystallisation interaction points. When the annealing temperature is lower than T_B, considerable precipitation would occur before recrystallisation and thereby inhibit recrystallisation. When the annealing temperature is between T_B and T_A, recrystallisation and precipitation occur simultaneously. When the annealing temperature is higher than T_A, full recrystallisation occurs before precipitation [31,37]. The solvus temperature of the WE43 alloy used in this work was 525 °C. When the sample was annealed at 400 °C, only precipitation occurred, with no recrystallisation. Simultaneous precipitation and recrystallisation took place at annealing temperatures of 450 °C and 490 °C. Only recrystallisation occurred when the sample was annealed at 545 °C. Combining these results in the schematic, it was clear that 400 °C was below point B, while 450 °C and 490 °C were between points A and B, and 545 °C was above point A. Although solute drag can retard dynamic recrystallisation, it cannot inhibit static recrystallisation at high temperatures [22]. Therefore, it was the Zener pinning from the precipitation that retarded the static recrystallisation at 400 °C. When the annealing temperature was increased to 450 °C and 490 °C, recrystallisation occurred in the shear bands, but the grain boundaries were pinned, resulting in a random texture (Fig. 13(a−l)). When the sample was annealed above the solvus temperature at 545 °C, neither segregation nor precipitation occurred. Therefore, the grain growth at this temperature was a result of the intrinsic character of grain boundaries: the grain boundary mobility of off-basal grains was faster than basal grains when they consume deformed grains [4,23,38], as shown in Fig. 13(m−r). Most off-basal grains were larger than the average grain size and these grew more rapidly than the smaller basal oriented grains. This difference resulted in a non-basal texture after full recrystallisation annealing at 545 °C (Fig. 13(p)).

Intense shear bands have often been observed in non-RE alloys [15,26], but most of them still exhibited a basal texture after recrystallisation. In these alloys, solute drag and Zener pinning
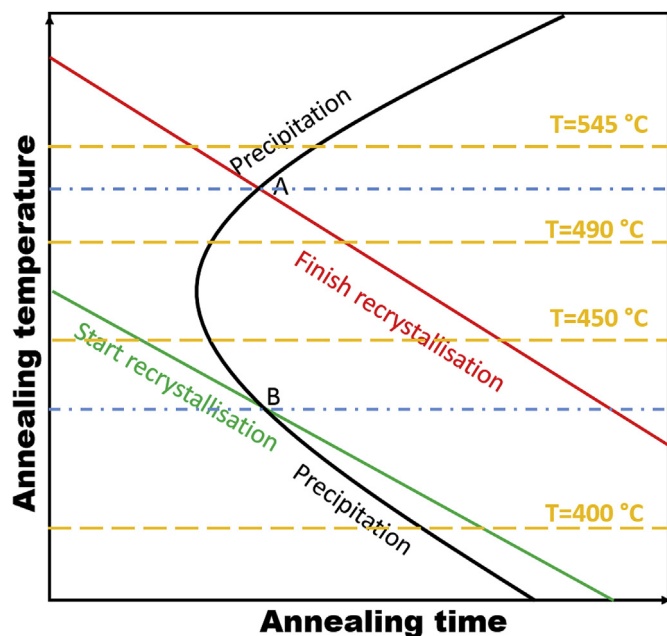
could be excluded as contributing to texture. Non-RE elements such as Al and Zn with small atom size and high diffusion rate do not segregate strongly to grain boundaries compared to RE elements such as Gd and Y with large atom size and low diffusion rate [22,24]. Moreover, Robson et al. [22] reported different RE elements resulted in different recrystallised textures. In a Mg-Y alloy, strong segregation to grain boundaries and weakened texture was observed after recrystallisation. In a Mg-Nd alloy, no solute segregation, or weakened texture was detected after recrystallisation due to low solubility of Nd in Mg and insoluble particles formed with impurities. Basu et al. [25] also compared the different recrystallisation texture evolution responses of Mg-Gd and Mg-Dy alloys at various annealing temperatures. Gd exhibited a considerably larger tendency to segregate in comparison with Dy due to different segregation energies. On the other hand, non-basal texture or RE texture was not formed during recrystallisation when strong solute drag was present along grain boundaries [21]. For example, a basal texture has been observed in a Mg-Ca alloy where strong segregation of Ca was found. Moreover, it is still not clear whether solute segregation occurs globally or only along specific types of grain boundaries (e.g., high angle grain boundaries). Therefore, it is not clear whether the extent of solute drag depends on the boundary type.

As shown in Fig. 13, WE43 alloy annealed at 545 °C, where we have shown there was limited solute drag or particle pinning effect, exhibited a non-basal texture formed from shear band recrystallisation. This indicates other factors, such as the density and distribution of shear bands, as with double twins discussed in Ref. [20], need to be taken into account when determining how much they contributed to the full recrystallised texture.

In pure Mg and non-RE alloys, shear bands are found to be heterogeneously distributed in a few coarse bands [5,15]. The recrystallisation process involves competitive growth from the different nucleation sites. The most common nucleation site is at prior grain boundaries, provided their mobility is not reduced by solute drag or precipitate pinning. Recrystallised grains originating from shear bands do not usually grow beyond the shear band in which they originated, and therefore, their contribution to the final texture depends on the volume fraction of shear bands. However, recrystallised grains produced by SIBM consume the deformed matrix more quickly thereby limiting the contribution to texture from the recrystallised shear bands. As an example, Fig. S8 provides grain growth analysis by using *quasi-in-situ* EBSD in a cold-rolled AZ31 Mg alloy. Regions within deformation bands recrystallised and grew quickly after annealing at 350 °C for 270s compared to the grain boundary. However, after annealing 1290s, grains within deformation bands lost their growth advantage and were restricted by deformation band boundaries. The grains with green and orange colouration nucleated at grain boundaries showed a much faster grain and spread quickly and freely to consume parent grains. Therefore, the contribution of grain boundary recrystallisation to recrystallised texture would be magnified, while the contribution from deformation bands would be reduced with increasing annealing time. This effect would be more significant with smaller grain size because of high volume fraction of prior grain boundaries.

In contrast to RE free Mg alloys, a high density of shear bands is usually generated in Mg-RE alloys, which tend to be much more uniformly distributed than in RE free alloys. This inevitably means that recrystallisation within the shear bands will contribute much more to the final texture, as was the case here (Fig. 1(b−d)). Moreover, the homogeneous distribution of shear bands meant that recrystallised grains from shear bands were able to grow into the deformed matrix. These combined effects improved the competitiveness of shear band recrystallisation over SIBM recrystallisation.

Fig. 14. A schematic for illustrating the interactions of precipitation and recrystallisation during isothermal annealing, adapted from Ref. [31].

The non-basal orientations produced by shear band recrystallisation dominated subsequent grain growth, which resulted in the formation of non-basal texture.

5. Conclusions

The recrystallisation process from nucleation to full recrystallisation was investigated using *quasi-in-situ* EBSD. The individual effect of shear bands on texture evolution was systematically investigated, and key conclusions were drawn:

(1) Shear bands were the preferential nucleation sites and shear band recrystallisation was the main source of the observed recrystallised texture. Recrystallisation from deformation twins occupied a negligible amount of the final recrystallised area. This was due to the low density of deformation twins and intersections between these deformation twins.

(2) The texture observed from recrystallisation in the shear bands was relatively random, with a weakened basal component, and not a typical RE texture. This texture evolved as a result of a wide range of local misorientation of grains within shear bands.

(3) Precipitation and recrystallisation occurred simultaneously during annealing at 450 and 490 °C. These precipitates pinned the grain boundaries and retarded recrystallisation along grain boundaries, thereby reducing the source of a basal texture.

(4) The weakened basal texture with scattered weak texture components emerged during nucleation and was preserved during grain growth, so that no orientated grain growth was observed.

(5) When the sample was annealed at 545 °C, at which temperature solute drag and Zener pinning would have been negligible, a non-basal texture was obtained after full recrystallisation. Orientated grain growth was observed, which was governed by the grain boundary mobility.

(6) The density and distribution of shear bands had a strong influence on the final texture at temperatures where there was no pinning of grain boundaries by solute drag and Zener pinning. This explains why non-RE alloys that contain shear bands usually produce basal texture after recrystallisation.

(7) A large amount of RE additions is beneficial for age hardening in Mg-RE alloys, but could result in a detrimental effect in reducing the formation of a RE texture that is commonly observed in dilute Mg-RE alloys due to concurrent precipitation restricting preferable grain growth during recrystallisation.

Acknowledgements

Appendix A. Supplementary data

Supplementary data related to this article can be found at https://doi.org/10.1016/j.actamat.2017.12.019.

References

[1] A. Imandoust, C.D. Barrett, T. Al-Samman, K.A. Inal, H. El Kadiri, A review on the effect of rare-earth elements on texture evolution during processing of magnesium alloys, J. Mater. Sci. (2016) 1—29.

[2] T. Al-Samman, X. Li, Sheet texture modification in magnesium-based alloys by selective rare earth alloying, Mater. Sci. Eng. A 528 (2011) 3809—3822.

[3] J. Hirsch, T. Al-Samman, Superior light metals by texture engineering: optimized aluminum and magnesium alloys for automotive applications, Acta Mater. 61 (2013) 818—843.

[4] I. Basu, T. Al-Samman, G. Gottstein, Shear band-related recrystallization and grain growth in two rolled magnesium-rare earth alloys, Mater. Sci. Eng. A 579 (2013) 50—56.

[5] S. Sandlöbes, S. Zaefferer, I. Schestakow, S. Yi, R. Gonzalez-Martinez, On the role of non-basal deformation mechanisms for the ductility of Mg and Mg—Y alloys, Acta Mater. 59 (2011) 429—439.

[6] J.J. Bhattacharyya, S.R. Agnew, G. Muralidharan, Texture enhancement during grain growth of magnesium alloy AZ31B, Acta Mater. 86 (2015) 80—94.

[7] M.A. Steiner, J.J. Bhattacharyya, S.R. Agnew, The origin and enhancement of texture during heat treatment of rolled AZ31B magnesium alloys, Acta Mater. 95 (2015) 443—455.

[8] N. Stanford, M.R. Barnett, The origin of "rare earth" texture development in extruded Mg-based alloys and its effect on tensile ductility, Mater. Sci. Eng. A 496 (2008) 399—408.

[9] E.A. Ball, P.B. Prangnell, Tensile-compressive yield asymmetries in high strength wrought magnesium alloys, Scripta Metall. Mater. 31 (1994) 111—116.

[10] D. Griffiths, Explaining texture weakening and improved formability in magnesium rare earth alloys, Mater. Sci. Technol. 31 (2015) 10—24.

[11] D. Guan, W.M. Rainforth, L. Ma, B. Wynne, J. Gao, Twin recrystallization mechanisms and exceptional contribution to texture evolution during annealing in a magnesium alloy, Acta Mater. 126 (2017) 132—144.

[12] N. Stanford, D. Atwell, A. Beer, C. Davies, M.R. Barnett, Effect of microalloying with rare-earth elements on the texture of extruded magnesium-based alloys, Scr. Mercat. 59 (2008) 772—775.

[13] M. Sanjari, A. Farzadfar, A.S.H. Kabir, H. Utsunomiya, I.-H. Jung, R. Petrov, L. Kestens, S. Yue, Promotion of texture weakening in magnesium by alloying and thermomechanical processing: (I) alloying, J. Mater. Sci. 49 (2014) 1408—1425.

[14] J. Bohlen, M.R. Nürnberg, J.W. Senn, D. Letzig, S.R. Agnew, The texture and anisotropy of magnesium—zinc—rare earth alloy sheets, Acta Mater. 55 (2007) 2101—2112.

[15] L.W.F. Mackenzie, M.O. Pekguleryuz, The recrystallization and texture of magnesium—zinc—cerium alloys, Scr. Mercat. 59 (2008) 665—668.

[16] X. Huang, K. Suzuki, Y. Chino, Static recrystallization behavior of hot-rolled Mg-Zn-Ce magnesium alloy sheet, J. Alloy. Comp. 724 (2017) 981—990.

[17] J.D. Robson, D.T. Henry, B. Davis, Particle effects on recrystallization in magnesium—manganese alloys: particle-stimulated nucleation, Acta Mater. 57 (2009) 2739—2747.

[18] I. Basu, T. Al-Samman, Twin recrystallization mechanisms in magnesium-rare earth alloys, Acta Mater. 96 (2015) 111—132.

[19] P. Hidalgo-Manrique, S.B. Yi, J. Bohlen, D. Letzig, M.T. Pérez-Prado, Effect of Nd additions on extrusion texture development and on slip activity in a Mg-Mn alloy, Metall. Mater. Trans. A 44 (2013) 4819—4829.

[20] D. Guan, W.M. Rainforth, J. Gao, J. Sharp, B. Wynne, L. Ma, Individual effect of recrystallisation nucleation sites on texture weakening in a magnesium alloy: Part 1- double twins, Acta Mater. 135 (2017) 14—24.

[21] Z.R. Zeng, Y.M. Zhu, S.W. Xu, M.Z. Bian, C.H.J. Davies, N. Birbilis, J.F. Nie, Texture evolution during static recrystallization of cold-rolled magnesium alloys, Acta Mater. 105 (2016) 479—494.

[22] J. Robson, Effect of rare-earth additions on the texture of wrought magnesium alloys: the role of grain boundary segregation, Metall. Mater. Trans. A 45 (2014) 3205—3212.

[23] I. Basu, T. Al-Samman, Triggering rare earth texture modification in magnesium alloys by addition of zinc and zirconium, Acta Mater. 67 (2014) 116—133.

[24] J.D. Robson, S.J. Haigh, B. Davis, D. Griffiths, Grain boundary segregation of rare-earth elements in magnesium alloys, Metall. Mater. Trans. A 47 (2016) 522—530.

[25] I. Basu, K.G. Pradeep, C. Mießen, L.A. Barrales-Mora, T. Al-Samman, The role of atomic scale segregation in designing highly ductile magnesium alloys, Acta Mater. 116 (2016) 77—94.

[26] M.R. Barnett, M.D. Nave, C.J. Bettles, Deformation microstructures and textures of some cold rolled Mg alloys, Mater. Sci. Eng. A 386 (2004) 205—211.

[27] J.W. Senn, S.R. Agnew, Texture randomization of magnesium alloys containing rare earth elements, in: M.O. Pekguleryuz, N.R. Neelameggham, R.S. Beals, E.A. Nyberg (Eds.), Magnesium Technology, vol. 2008, 2008, pp. 153—158.

[28] J.W. Senn, S.R. Agnew, Texture randomization during thermomechancial processing of a magnesium-yttrium-neodymium alloy, in: L.W.F. Mackenzie (Ed.), Proceedings of Magnesium Technology in the Global Age, 2006, pp. 115—130.

[29] D. Guan, J. Nutter, J. Sharp, J. Gao, W. Mark Rainforth, Direct observation of precipitation along twin boundaries and dissolution in a magnesium alloy annealing at high temperature, Scr. Mercat. 138 (2017) 39—43.

[30] K.Y. Zhu, D. Chaubet, B. Bacroix, F. Brisset, A study of recovery and primary recrystallization mechanisms in a Zr—2Hf alloy, Acta Mater. 53 (2005) 5131—5140.

[31] F.J. Humphreys, M. Hatherly, Recrystallization and Related Annealing Phenomena, Elsevier Science, 2004.

[32] P.A. Beck, P.R. Sperry, Strain induced grain boundary migration in high purity aluminum, J. Appl. Phys. 21 (1950) 150—152.

[33] J.D. Robson, C. Paa-Rai, The interaction of grain refinement and ageing in magnesium—zinc—zirconium (ZK) alloys, Acta Mater. 95 (2015) 10—19.

[34] H. Somekawa, T. Mukai, Effect of grain boundary structures on grain boundary

sliding in magnesium, Mater. Lett. 76 (2012) 32—35.

[35] J. Bohlen, S. Yi, D. Letzig, K.U. Kainer, Effect of rare earth elements on the microstructure and texture development in magnesium—manganese alloys during extrusion, Mater. Sci. Eng. A 527 (2010) 7092—7098.

[36] N. Stanford, D. Atwell, M.R. Barnett, The effect of Gd on the recrystallisation, texture and deformation behaviour of magnesium-based alloys, Acta Mater. 58 (2010) 6773—6783.

[37] M.J. Jones, F.J. Humphreys, Interaction of recrystallization and precipitation: the effect of Al3Sc on the recrystallization behaviour of deformed aluminium, Acta Mater. 51 (2003) 2149—2159.

[38] I.J. Polmear, Magnesium alloys and applications, Mater. Sci. Technol. 10 (1994) 1—16.